International Journal of Heat and Mass Transfer 261 (2026) 128523

Contents lists available at ScienceDirect

International Journal of Heat and Mass Transfer

journal homepage: www.elsevier.com/locate/hmt

Modeling of conjugate forced convection using effective boundary conditions: From plane channel to the human nose

Eric Segalerba [a,*,1], Essam Nabil Ahmed [a,2,3], Maria Vittoria Pennisi [b,3], Maurizio Quadrio [b,3], Jan Oscar Pralits [a,*]

[a] Dipartimento di Ingegneria Civile, Chimica e Ambientale, Università di Genova, via Montallegro 1, 16145, Genova, Italy
[b] Dipartimento di Scienze e Tecnologie Aerospaziali, Politecnico di Milano, via La Masa 34, 20156, Milano, Italy

ARTICLE INFO

Keywords:
Conjugate heat convection
Corrugated channels
Nasal flow aerodynamics
Multiscale homogenization
Effective boundary conditions

ABSTRACT

Accurate analysis of conjugate heat transfer (CHT) is of primary importance in many engineering applications and biological flows where it is crucial to implement a reliable model that couples thermal conduction in the solid boundary with convection in the fluid. CHT simulations entail higher computational costs to well resolve the smooth/rough solid layers and to generate high-quality meshes for complex finite-thickness wall geometries. This work adopts upscaled boundary conditions capable of modeling the heat transfer at a fraction of the cost of the full conjugate-forced-convection analysis. The effective velocity and temperature conditions are applied to pressure-driven, developing flows through ducts with different types of wall roughness down to the smooth limit. The results are compared against fully resolving CHT simulations, and the good agreement demonstrates suitability of the macroscopic approach as a cheaper alternative. The model is finally applied to the flow within the human nose, where CHT is mandatory because of the physiological importance of thermal exchange processes. Despite the simplifying assumptions made to the physics in this case, the results obtained are fairly encouraging for future use of the model, possibly with relevant adjustments and extensions, in typical biomedical contributions.

1. Introduction

Conjugate heat transfer (CHT) is of primary importance in many engineering applications spanning from efficient heat transfer in heat exchangers to insulation for energy-saving systems or for electrical cooling devices. It consists of coupled heat transfer processes taking place simultaneously in two domains having a shared boundary, i.e., the solid/fluid interface; the heat transfer regimes incorporated are, thus, the thermal conduction through the solid layer and the convective heat transfer to the working fluid [1]. When the solid is thin, compared to the characteristic length of the fluid domain, and the thermal conductivity ratio between the solid and the fluid is large, as in the case of metal and air, the temperature at the solid/fluid interface is roughly equal to that at the base surface of the solid layer. On the other hand, when the thermal conductivity ratio is moderate, at most one or two orders of magnitude, the interface temperature could have substantial variations. Such a scenario is encountered, for instance, considering the air motion in the human upper airways, trachea, and lungs and the blood flow in the thin vessels throughout the human body. The solid in these cases is represented by the mucosa, human tissue, and endothelial cells for which the thermal conductivity is roughly that of water. Bypassing the analysis of thermal conduction in the solid domain by assuming a simple boundary condition at the solid/fluid interface, such as a uniform temperature, is advantageous in terms of the computational cost since this allows us to focus on convective heat transfer in the fluid as a decoupled problem. Nonetheless, performing a CHT analysis of a thermal system is indispensable whenever the level of accuracy of the predictions is crucial and/or a detailed understanding of the physical phenomena is sought. This applies to a large number of industrial activities [2–4] as well as biological applications [5,6]. Upscaling approaches constitute an easier alternative to the conventional full feature-resolving simulations when hierarchical flow problems are numerically analyzed. The hydrodynamic/thermal interaction between

* Corresponding authors.
E-mail addresses: esegalerba@unisa.it (E. Segalerba), essameldin.nabilahmedkamalabdo@imft.fr (E.N. Ahmed), mariavittoria.pennisi@mail.polimi.it (M.V. Pennisi), maurizio.quadrio@polimi.it (M. Quadrio), jan.pralits@unige.it (J.O. Pralits).
[1] Present address: Department of Industrial Engineering (DIIN), University of Salerno, Fisciano 84084, Italy.
[2] Present address: Institut de Mécanique des Fluides de Toulouse (IMFT), University of Toulouse, CNRS, 31400 Toulouse, France.
[3] Contributing author(s).

https://doi.org/10.1016/j.ijheatmasstransfer.2026.128523
Received 31 October 2025; Received in revised form 12 January 2026; Accepted 9 February 2026
Available online 17 February 2026

a fluid and a perturbed boundary is a typical example in which upscaling can be viable, provided that the characteristic length scale of the surface texture (ℓ) is sufficiently smaller than that of the large-scale flow structures ($\mathcal{L}$). The multiscale homogenization technique, employed in this paper, yields homogeneous macroscopic parameters (such as the Navier-slip length and the thermal-slip coefficient) which replace the rapidly varying properties related to the heterogeneous microstructure of the physical surface which can be, *inter alia*, corrugated, rough, or permeable [7–9]. The upscaled parameters can be evaluated by solving derived *auxiliary* systems of partial differential equations that govern the distributions of *closure* variables in a microscopic unit cell [10–14]. The estimated model coefficients directly contribute to *effective* boundary conditions at a virtual plane interface next to the rough boundary; this allows us to study the macroscale problem beyond the fictitious interface chosen (for example, the one passing through the crests of the roughness elements) and, hence, to eschew the numerical resolution of the fully-featured fields between/through/close to the surface corrugations/protrusions, a clear advantage when reasonable accuracy at a reduced computational cost is a priority. In recent years, the development of robust homogenization-based models has been the subject of several investigations. In respect of hierarchical conjugate heat transfer problems, Ahmed et al. [13] and Ahmed and Tanda [14] studied conjugate natural convection along a heated vertical wall regularly roughened with ribs having finite values of the thermal conductivity (in addition to perfectly conductive or adiabatic elements as the two limiting situations); effective velocity and temperature boundary conditions at the microscopic/macroscopic interface were formulated, implemented and successfully validated for several surface textures and thermal conditions.

The CHT-related problem of nasal airflow is one of the cases of interest in this work. Besides transferring air from the environment to the lungs, the human nose performs many functions related to airflow conditioning; its inner geometry maximizes the surface-to-volume ratio for cleaning, moisturizing, and regulating the warming and cooling of the air. The regimes involved in thermal regulation are the conductive heat transfer in the stationary mucous layer bounding the internal air passage, the heat transfer by forced convection to the air, and the latent heat whose effect pertains to the moisturizing function of the nose [15–18]. The thermal conductivity of the mucous layer is similar to that of water, which renders the mucous-layer-to-air thermal conductivity ratio moderate. This may necessitate a full CHT analysis towards a higher fidelity of the temperature distribution and the heat transfer rate, instead of imposing a Dirichlet, or Neumann, boundary condition of the temperature at the mucus/air interface. Nonetheless, by surveying the existing literature [16,19–22] on this topic, it can be found that the latter simplified approach is enforced in several CFD simulations with a constant mucosal temperature whose value differs from one study to another within a typical range of 305.8 K–307.2 K. The higher accuracy guaranteed by the fine-grained simulations comes at a price: the computational requirements are more expensive since (i) the stationary layer is to be considered and properly meshed for an accurate numerical solution of Laplace equation governing the spatial distribution of the temperature through it, (ii) a coupling should be performed at the interface between the two sub-domains at each iteration so that the temperature and the heat flux are matched. The interested reader can refer to [23] for additional information on applied and theoretical aspects of conjugate heat transfer. In addition, pre-processing the full domain in this case can be a very challenging undertaking: the geometric complexity of the upper airways causes issues when the thin solid domain (representing the mucous layer) is added, since self-intersections can occur. As a consequence, it is often necessary to simplify the original geometry, thereby losing details, in order to obtain numerically stable and converged solutions. Finally, it is worth highlighting that one needs to handle a number of issues related to the data acquired from the original computed tomography (CT) scan such as resolution, smoothing, definition of the solid surface, etc. In this scenario, providing accurate boundary conditions able to mimic the presence of the stationary layer can be a very efficient practice. The work first examines the application of effective velocity and temperature boundary conditions to hydrodynamically and thermally developing, pressure-driven flows through channels bounded by rib-roughened heated walls, and up to our best knowledge this is the first contribution that considers this scenario with homogenization. Second, we introduce a simplified version of the model for the limiting case of a smooth channel (possibly wavy) with a preferential thermal conduction path, and apply it to the flow in several ducts to evaluate the effect of wall curvature, convergence/divergence, and laminar/turbulent conditions. Subsequently, we examine its applicability in the case of CHT in nasal airflow. It is important to point out that the latent heat related to moisturizing in the nose is not modeled since we are focusing the analysis on the conductive–convective heat transfer problem. Hence, we do not claim that the results shown here for the nasal airflow represent a complete biomedical contribution, yet they demonstrate the potentiality of the macroscopic model as a cheaper alternative to the full CHT analysis and encourage for future use of the approach, possibly with more physics incorporated. (Note: the work on a new model that incorporates latent heat and humidity is ongoing.) The paper is structured as follows. In Section 2, the physical problem is described, the underpinning of the upscaling approach is outlined, and the effective boundary conditions as well as the closure problems are stated. In Section 3, the homogenization-based numerical simulations are validated against full feature-resolving ones for the conjugate forced convection associated with developing flows in simple ducts, channels with rough boundaries, and complex channels with a preferential heat transfer path such as the case of the human nose. Discussion and conclusions are provided in Sections 4 and 5, respectively.

2. Problem definition and homogenization procedure

2.1. The fully resolving numerical simulations

The complex hydrodynamic and thermal interaction between a fluid flowing in a channel (externally forced in $\hat{x}$) and the periodically textured/corrugated delimiting boundaries is considered, as illustrated in Fig. 1(*a*). The conjugate heat transfer problem, including thermal conduction in the stationary boundaries and heat transfer by forced convection to the fluid phase, is numerically analyzed. The dimensional mass, momentum, and energy conservation equations governing the steady, incompressible, Newtonian flow at any point $(\hat{x}_1, \hat{x}_2, \hat{x}_3) = (\hat{x}, \hat{y}, \hat{z})$ in the fluid domain (β) are, respectively,

$$\frac{\partial \hat{u}_i}{\partial \hat{x}_i} = 0, \tag{1}$$

$$\rho\, \hat{u}_j \frac{\partial \hat{u}_i}{\partial \hat{x}_j} = -\frac{\partial \hat{P}}{\partial \hat{x}_i} + \mu \frac{\partial^2 \hat{u}_i}{\partial \hat{x}_j^2}, \tag{2}$$

$$\hat{u}_j \frac{\partial \hat{T}}{\partial \hat{x}_j} = \left(\frac{k_f}{\rho c_p}\right) \frac{\partial^2 \hat{T}}{\partial \hat{x}_j^2}, \tag{3}$$

with $\hat{\mathbf{u}}$ the velocity vector, $\hat{P}$ the pressure and $\hat{T}$ the temperature. The fluid properties, i.e., the density ρ, the dynamic viscosity μ, the thermal conductivity k_f, and the specific heat c_p, are assumed constant, neglecting variations in their values with temperature along and across the channel. Moving to the solid bounding layers (σ), the steady thermal conduction is governed by the following Laplace's equation describing spatial variations of the temperature $\hat{T}$:

$$\frac{\partial^2 \hat{T}}{\partial \hat{x}_j^2} = 0. \tag{4}$$

A uniform, prescribed temperature $\hat{T}_C$ is imposed at the outer surfaces (I_C) of the bounding plates, i.e., at $\hat{x}_2 = -e$ (for lower layer) and $\hat{x}_2 = h + H + h' + e'$ (for upper layer), while the side surfaces of the plates orthogonal to $\hat{x}_1 = \hat{x}$ (those located at the channel inlet/outlet

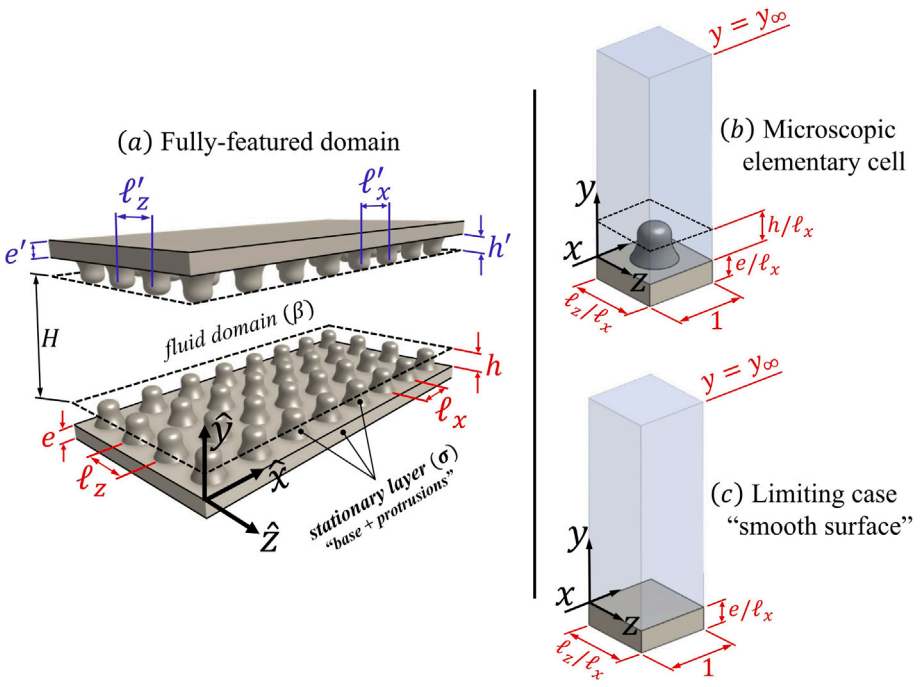

Fig. 1. Sketch of the problem under consideration. The plane interfaces delimited by dashed lines constitute the *virtual boundaries* where effective conditions are to be enforced.

and indicated hereafter as $\mathcal{I}_{ad}$) are assumed adiabatic. Continuity of temperature and heat flux is defined along the solid–fluid interfaces ($\mathcal{I}_{\sigma\beta}$). The aforementioned boundary conditions can be expressed as follows:

$$\begin{cases} \hat{T} = \hat{T}_C & \text{at } \mathcal{I}_C, \\ \dfrac{\partial \hat{T}}{\partial \hat{x}_1} = 0 & \text{at } \mathcal{I}_{ad}, \\ \hat{T} = \hat{T}, \quad \dfrac{\partial \hat{T}}{\partial \hat{n}} = \kappa \dfrac{\partial \hat{T}}{\partial \hat{n}} & \text{at } \mathcal{I}_{\sigma\beta}, \end{cases} \tag{5}$$

with $\kappa = \dfrac{k_s}{k_f}$ the solid-to-fluid thermal conductivity ratio and $\hat{n}$ the dimensional distance in the direction normal to $\mathcal{I}_{\sigma\beta}$ at any point. In addition, the fluid is assumed to enter the channel at a uniform velocity $\hat{u}_1\big|_{\hat{x}_1=0} = \hat{u}_{inlet}$ and temperature $\hat{T}\big|_{\hat{x}_1=0} = \hat{T}_{inlet}$, and a no-slip velocity boundary condition is enforced at $\mathcal{I}_{\sigma\beta}$, while the static pressure is set to zero at the outlet. The fields are periodic in the spanwise direction, $\hat{x}_3 = \hat{z}$.

2.2. The homogenization-based upscaling

The fine-grained analysis described above is capable of resolving the fully-featured fields in the fluid and the solid domains; however, when the macroscale behavior of channel flow is of particular interest, it is advantageous from the computational point of view to implement an upscaling approach that mimics the presence of the rough walls via the application of effective velocity and temperature boundary conditions at fictitious plane interfaces next to the physical boundaries. In the present work, we adopt a multiscale homogenization approach similar to that derived, validated, and upgraded in [12–14], except that forced, instead of natural, convection is considered here, and therefore the buoyancy has no contribution to the problem. In the homogenization-based simulations, the macroscopic variables ($\ddot{u}_i$, $\ddot{P}$, $\ddot{T}$) are targeted through the fluid domain bounded by the virtual interfaces; these fields correspond, if accurately evaluated, to the running averages ($\langle\hat{u}_i\rangle$, $\langle\hat{P}\rangle$, $\langle\hat{T}\rangle$) of the fully-featured variables resolved in the fine-grained simulations ($\hat{u}_i$, $\hat{P}$, $\hat{T}$). By considering the case of a wall roughened with protrusions of pitch distances ℓ_x and ℓ_z (refer to Fig. 1(*a*)) as a representative example, one can define the running-average temperature at a point $\Psi : (\hat{x}_\psi, \hat{y}_\psi, \hat{z}_\psi)$, located in the fluid domain beyond the roughness layer, by averaging the fully-resolved field over a rectangular $\hat{x} - \hat{z}$ region of dimensions $\ell_x \times \ell_z$, whose center is the point Ψ, as follows:

$$\langle T\rangle\big|_{\hat{x}_\psi,\hat{y}_\psi,\hat{z}_\psi} = \frac{1}{\ell_x \times \ell_z} \int_{\hat{x}_\psi-\ell_x/2}^{\hat{x}_\psi+\ell_x/2} \int_{\hat{z}_\psi-\ell_z/2}^{\hat{z}_\psi+\ell_z/2} \hat{T}(\hat{x}_\psi, \hat{y}_\psi, \hat{z}_\psi)\, d\hat{z}\, d\hat{x} \approx \ddot{T}\big|_{\hat{x}_\psi,\hat{y}_\psi,\hat{z}_\psi}, \tag{6}$$

and likewise for the velocity and pressure. While the typical interaction between the forced flow and the roughness elements is generally three-dimensional, and the fully-resolved velocity field is three-directional (taking into account spanwise deflection of the streamlines around the protrusions), the problem can be considered two-dimensional from the macroscopic point of view, including development of the viscous and thermal boundary layers along the streamwise direction, $\hat{x}_1$, and variations of the fields in the wall-normal direction, $\hat{x}_2$. Moreover, the macroscopic (averaged) spanwise velocity component, $\ddot{u}_3 = 0$, is expected to vanish, provided that the microscopic pattern of the textured boundaries has no preferential orientation relative to the direction of the external forcing, as in the case sketched in Fig. 1, or preferentially oriented at an angle of either 0 or 90 degrees, as in the case of streamwise-elongated (longitudinal) or spanwise-elongated (transverse) roughness elements; the reader is encouraged to refer to [24,25] for further discussions/elaboration. In view of the above-mentioned simplifications, it is sufficient to run the homogenization-based simulation over a two-dimensional ($\hat{x}_1 - \hat{x}_2$) plane through which the fields $\ddot{u}_1$, $\ddot{u}_2$, and $\ddot{T}$ are to be evaluated. The spatial variations of these variables are governed by

$$\frac{\partial \ddot{u}_i}{\partial \hat{x}_i} = 0, \tag{7}$$

$$\rho\, \ddot{u}_j \frac{\partial \ddot{u}_i}{\partial \hat{x}_j} = -\frac{\partial \ddot{P}}{\partial \hat{x}_i} + \mu \frac{\partial^2 \ddot{u}_i}{\partial \hat{x}_j^2}, \tag{8}$$

$$\ddot{u}_j \frac{\partial \ddot{T}}{\partial \hat{x}_j} = \left(\frac{k_f}{\rho c_p}\right) \frac{\partial^2 \ddot{T}}{\partial \hat{x}_j^2}, \tag{9}$$

subject to *effective* boundary conditions of $\ddot{u}_1$, $\ddot{u}_2$, and $\ddot{T}$ along the virtual interfaces, chosen here at $\hat{x}_2 = h$ and $\hat{x}_2 = h+H$, i.e., the planes passing by the tips/crests of the protrusions. These upscaled conditions are already available in the literature (with simple adjustment) via application of the asymptotic homogenization [13,14], and their validity is contingent on the presence of well-separated length scales (for instance, the pitch distance of the roughness pattern, ℓ, as a microscopic length scale and the channel height, H, as a macroscopic length scale), such that a small parameter, $\epsilon = \ell/H \ll 1$, can be defined. Under steady flow conditions, we neglect the transpiration velocity at the fictitious interfaces by setting $\ddot{u}_2\big|_{\hat{x}_2=h}$ and $\ddot{u}_2\big|_{\hat{x}_2=h+H}$ to *zero*, while the following boundary conditions of $\ddot{u}_1$ and $\ddot{T}$, second-order accurate in terms of ϵ, are imposed:

$$\ddot{u}_1\Big|_{\hat{x}_2=h} \approx \Lambda_x^{(b)} \frac{\partial \ddot{u}_1}{\partial \hat{x}_2}\Big|_{\hat{x}_2=h} + \frac{M_{12}^{(b)}}{\mu} \frac{\partial}{\partial \hat{x}_1}\left(-\ddot{P} + 2\mu \frac{\partial \ddot{u}_2}{\partial \hat{x}_2}\right)\Bigg|_{\hat{x}_2=h}, \tag{10}$$

$$\ddot{T}\Big|_{\hat{x}_2=h} \approx \hat{\mathcal{T}}_C + \Lambda_\theta^{(b)} \frac{\partial \ddot{T}}{\partial \hat{x}_2}\Big|_{\hat{x}_2=h}, \tag{11}$$

and for the top interface,

$$\ddot{u}_1\Big|_{\hat{x}_2=h+H} \approx -\Lambda_x^{(t)} \frac{\partial \ddot{u}_1}{\partial \hat{x}_2}\Big|_{\hat{x}_2=h+H} + \frac{M_{12}^{(t)}}{\mu} \frac{\partial}{\partial \hat{x}_1}\left(-\ddot{P} + 2\mu \frac{\partial \ddot{u}_2}{\partial \hat{x}_2}\right)\Bigg|_{\hat{x}_2=h+H}, \tag{12}$$

$$\ddot{T}\Big|_{\hat{x}_2=h+H} \approx \hat{\mathcal{T}}_C - \Lambda_\theta^{(t)} \frac{\partial \ddot{T}}{\partial \hat{x}_2}\Big|_{\hat{x}_2=h+H}, \tag{13}$$

where the model parameters Λ_x, Λ_θ, and M_{12} are the dimensional Navier-slip, thermal-slip, and interface permeability coefficients, respectively, and they are defined for the bottom (superscript b) and top (superscript t) boundaries. These upscaled coefficients correspond to the product of their dimensionless counterparts (λ_x, λ_θ, and m_{12}) times either a length (for the slip parameters) or a surface area (for the interface permeability) as follows:

$$\Lambda_x^{(b)} = \lambda_x^{(b)} \ell_x, \quad \Lambda_\theta^{(b)} = \lambda_\theta^{(b)} \ell_x, \quad M_{12}^{(b)} = m_{12}^{(b)} \ell_x^2, \tag{14}$$

$$\Lambda_x^{(t)} = \lambda_x^{(t)} \ell'_x, \quad \Lambda_\theta^{(t)} = \lambda_\theta^{(t)} \ell'_x, \quad M_{12}^{(t)} = m_{12}^{(t)} \ell'^2_x, \tag{15}$$

taking into account that, in this formulation, the pitch distances ℓ_x and ℓ'_x (indicated in Fig. 1) are chosen as the microscopic length scales of the bottom and the top walls, respectively. It is important to highlight that the homogenization-based model is free of any empirical parameters since the dimensionless macroscopic coefficients of interest can be evaluated by solving *ad hoc* auxiliary problems governing the distribution of closure variables over an elementary cell, representative of the microscopic domain, with the dimensions normalized by the microscopic length scale as sketched in Fig. 1(*b*). The dimensionless microscopic coordinates $x_i = \hat{x}_i/\ell_x$ are thus defined at the bottom wall, and likewise for the top surface except that ℓ'_x is to be used for normalization and the vertical coordinate is to be reversed such that it points away from the wall. In particular, it is sufficient at each boundary to solve one Stokes-like and one Laplace-like systems governing the auxiliary variables ($u_i^\dagger$, $p^\dagger$) and ($\theta^\dagger$, $\phi^\dagger$), respectively, in order to evaluate λ_x and m_{12} (based on $u_1^\dagger$) and λ_θ (based on $\theta^\dagger$). Such closure problems read

$$\begin{cases} \partial_i u_i^\dagger = 0 & \text{in fluid domain } (\beta), \\ -\partial_i p^\dagger + \partial_j^2 u_i^\dagger = 0 & \text{in fluid domain } (\beta), \\ -p^\dagger \delta_{i2} + \partial_2 u_i^\dagger + \partial_i u_2^\dagger = \delta_{i1} & \text{at } y = y_\infty, \\ u_i^\dagger = 0 & \text{at } \mathcal{I}_{\sigma\beta}, \end{cases} \tag{16}$$

and

$$\begin{cases} \partial_i^2 \theta^\dagger = 0 & \text{in fluid domain } (\beta), \\ \partial_i^2 \phi^\dagger = 0 & \text{in solid domain } (\sigma), \\ \partial_2 \theta^\dagger = 1 & \text{at } y = y_\infty, \\ \theta^\dagger = \phi^\dagger, \ \frac{\partial \theta^\dagger}{\partial n} = \kappa \frac{\partial \phi^\dagger}{\partial n} & \text{at } \mathcal{I}_{\sigma\beta}, \\ \phi^\dagger = 0 & \text{at } \mathcal{I}_C, \end{cases} \tag{17}$$

plus periodicity of all the dependent variables in the x and z directions. The operators used above are defined as $\partial_i = \dfrac{\partial}{\partial x_i}$ and $\partial_i^2 = \dfrac{\partial^2}{\partial x_i^2}$. The basic derivation requires that the closure problems are to be solved in a microscopic unit cell with the matching interface, at $y = y_\infty$, set sufficiently far from the wall (for instance, $y_\infty \approx 5$). However, the upscaled coefficients for a matching interface of choice at $y_\infty = h/\ell_x$ (i.e., the plane of crests) can be estimated directly from the following averaging operations:

$$\lambda_x = \frac{1}{\mathcal{A}_{xz}} \int_{\mathcal{S}_0} u_1^\dagger \, dA, \quad m_{12} = \frac{1}{\mathcal{A}_{xz}} \int_{\mathcal{V}_0} u_1^\dagger \, dV, \tag{18}$$

$$\lambda_\theta = \frac{1}{\mathcal{A}_{xz}} \int_{\mathcal{S}_0} \theta^\dagger \, dA, \tag{19}$$

where $\mathcal{S}_0$ and $\mathcal{V}_0$ are, respectively, the virtual surface at and the fluid volume below the plane $y = h/\ell_x$, and $\mathcal{A}_{xz}$ is the normalized area of an $x-z$ cross section of the unit cell ($\mathcal{A}_{xz} = 1 \times \dfrac{\ell_z}{\ell_x}$). Clearly, the systems (16) and (17), together with the relations (18) and (19), render the coefficients λ_x and m_{12} dependent merely on the geometric details of the wall texture, whereas the thermal-slip coefficient λ_θ depends, in addition, on the solid-to-fluid thermal conductivity ratio, κ. Values of these parameters are available in Refs. [12,13,25,26] for rough boundaries of different geometric/thermal characteristics.

2.3. The smooth-channel limiting case

For the limiting case of a channel flow bounded by a smooth wall of finite thickness, e, and finite value of thermal conductivity, k_s, we can find analytical solutions for the closure variables $u_1^\dagger$ and $\theta^\dagger$ from the auxiliary systems (16) and (17), respectively, and thus to directly evaluate the macroscopic coefficients λ_x, m_{12}, and λ_θ which contribute to the effective boundary conditions at the smooth boundary of the channel. This is possible since, in the absence of surface protrusions, the closure fields are all uniform in the streamwise (x) and spanwise (z) directions; the problems governing the distributions of $u_1^\dagger$ and $\theta^\dagger$ in a microscopic unit cell (Fig. 1(*c*)) now read

$$\begin{cases} \partial_2^2 u_1^\dagger = 0 & \text{in } \beta \\ \partial_2 u_1^\dagger = 1 & \text{at } y = y_\infty \\ u_1^\dagger = 0 & \text{at } \mathcal{I}_{\sigma\beta} \ (y = 0) \end{cases}, \quad \begin{cases} \partial_2^2 \theta^\dagger = 0 & \text{in } \beta \\ \partial_2^2 \phi^\dagger = 0 & \text{in } \sigma \\ \partial_2 \theta^\dagger = 1 & \text{at } y = y_\infty \\ \theta^\dagger = \phi^\dagger, \ \partial_2 \theta^\dagger = \kappa \, \partial_2 \phi^\dagger & \text{at } \mathcal{I}_{\sigma\beta} \ (y = 0) \\ \phi^\dagger = 0 & \text{at } \mathcal{I}_C \ (y = -e/\ell) \end{cases}. \tag{20}$$

Integrating the governing equations twice and evaluating the integration constants via application of the boundary conditions, we find the following closed-form solutions in the fluid domain β:

$$u_1^\dagger = y, \qquad \theta^\dagger = y + \frac{e}{\ell \times \kappa}. \tag{21}$$

Hence, the macroscopic coefficients for the smooth interface at $y = 0$ are

$$\lambda_x, \, m_{12} = 0, \qquad \lambda_\theta = \frac{e}{\ell \times \kappa}. \tag{22}$$

and their dimensional counterparts are

$$\Lambda_x, \, M_{12} = 0, \qquad \Lambda_\theta = \frac{e}{\kappa}, \tag{23}$$

which means that, for the smooth, impermeable boundary, the no-slip velocity boundary condition is retrieved (which is clear a priori), while the following Robin boundary condition arises:

$$\ddot{T}\Big|_{\hat{n}=0} \approx \hat{\mathcal{T}}_C + \frac{e}{\kappa} \times \frac{\partial \ddot{T}}{\partial \hat{n}}\Big|_{\hat{n}=0}. \tag{24}$$

Thus, the temperature at the inner surface of the wall $\ddot{T}\big|_{\hat{n}=0}$ (that is, the surface exposed to the working fluid) deviates from the reference uniform value $\hat{\mathcal{T}}_C$ imposed at the outer surface by a thermal slip whose

amount depends on the wall thickness (e), the solid-to-fluid thermal conductivity ratio (κ), and the normal temperature gradient at the inner surface. The dimensional distance $\hat{n}$ is defined along the direction normal to the solid–fluid interface in such a way that $\hat{n}$ increases while moving towards the fluid. In other words, if the condition is to be imposed at the lower (respectively upper) smooth wall, $\frac{\partial \ddot{T}}{\partial \hat{n}}$ coincides with $\frac{\partial \ddot{T}}{\partial \hat{x}_2}$ (respectively $-\frac{\partial \ddot{T}}{\partial \hat{x}_2}$) at the boundary, according to the coordinate system adopted in Fig. 1. The following notes on the previous equation merit attention.

i. Condition (24) applies in the absence of roughness elements on the surface of interest, and therefore there is no longer a specific given value for the pitch distance since the smooth surface repeats itself at any chosen distance ℓ. A vanishingly small value $\ell \to 0$ can be taken such that the averaged temperature $\ddot{T}$ coincides with the local temperature $\hat{T}$, and thus the model predictions can be compared directly to the results of the fully resolving simulations, i.e., without applying spatial averaging to the latter. The local version of (24) is

$$\hat{T}\Big|_{\hat{n}=0} \approx \hat{\mathcal{T}}_C + \frac{e}{\kappa} \times \frac{\partial \hat{T}}{\partial \hat{n}}\Big|_{\hat{n}=0} . \tag{25}$$

Although this approach is conceptually different from upscaling-based modeling (since no averaging is included now), we will nominally refer to the Robin boundary condition (25) as an effective condition, only in the sense that it is the limiting scenario of the effective model.

ii. If thermal conduction in the solid is one-directional, specifically across the thickness, condition (25) can be obtained, alternatively, by considering the fundamentals of heat transfer in the solid layer and at the solid–fluid interface ($\hat{n} = 0$). In this case, the temperature $\hat{\mathcal{T}}$ in the solid layer exhibits a linear distribution (and thus a constant gradient) along the thickness, leading to $\frac{\partial \hat{\mathcal{T}}}{\partial \hat{n}}\Big|_{\hat{n}=0} = (\hat{\mathcal{T}}|_{\hat{n}=0} - \hat{\mathcal{T}}_C)/e$. By applying the continuity of heat flux and temperature at $\hat{n} = 0$ (respectively, $\frac{\partial \hat{T}}{\partial \hat{n}}\Big|_{\hat{n}=0} = \kappa \frac{\partial \hat{\mathcal{T}}}{\partial \hat{n}}\Big|_{\hat{n}=0}$ and $\hat{T}|_{\hat{n}=0} = \hat{\mathcal{T}}|_{\hat{n}=0}$), the Robin boundary condition (25) can be eventually obtained.

iii. The previous point clarifies that condition (25) is valid when the normal direction is the preferential heat transfer path in the solid. One approach could be to judge validity based on smallness of the ratio between the wall thickness (e) and a macroscale longitudinal distance (for example, $\mathcal{L}_{th}$) over which a relatively significant temperature change takes place along the fluid-exposed surface of the boundary. The numerical analysis performed in this paper investigates accuracy simply by examining increasing values of e for given flow/channel configurations.

iv. It is worth anticipating that condition (25) will also be employed in the case of curved/undulating walls, for which the wall-normal direction (along which $\hat{n}$ is measured) varies from one point to another following the surface profile. When the surface is no longer flat, the validity of (25) is (in addition to what is mentioned in the previous point) contingent on the smallness of the ratio (Γ) between the wall thickness (e) and the radius of curvature of the wall (R, for example, average of the radii of the inner and outer surfaces of the wall of interest). In other words, for sufficiently small values of $\Gamma = e/R$ the curvilinear lengths of the inner and outer surfaces of the stationary wall can be assumed to be equal, and the boundary can thus be considered as flat. Again, increasing values of the thickness can be examined for a given configuration in order to monitor the deterioration of the model accuracy. In fact, a general condition (i.e., even for large Γ) that is valid for one-directional conduction across the thickness of known-curvature walls can be derived following the same lines given above in point (iii), where the only difference lies in the definition of $\frac{\partial \hat{\mathcal{T}}}{\partial \hat{n}}\Big|_{\hat{n}=0}$ (for example, refer to section 3.3.1 of Incorpera, DeWitt, Bergman and Lavine (2006) for the classical derivation of temperature distribution in a circular ring). However, we will use (25) in this work, keeping in mind its limitations, since we look forward to eventually applying the model to complex three-dimensional configurations like the nasal airflow, where acquiring the radii of curvature throughout the domain is a demanding undertaking.

3. Results

The main objective is to assess the ability of the homogenization-based effective boundary conditions, derived in Sections 2.2 and 2.3, to simplify the numerical analysis of conjugate forced convection in channels with different geometries of the bounding walls. In pursuit of validation, the temperature behaviors obtained through the homogenized model are compared against the results of classical fully resolving simulations considering different two-dimensional surface configurations before moving to the complex three-dimensional case of the human nasal airways. In all the problems investigated, we fix the properties of the flowing air $\rho = 1.293\ \frac{\text{kg}}{\text{m}^3}$, $\mu = 1.8 \times 10^{-5}\ \frac{\text{kg}}{\text{m s}}$, $k_f = 0.026\ \frac{\text{W}}{\text{m K}}$, and $c_p = 1004.9\ \frac{\text{J}}{\text{kg K}}$, the inlet temperature $\hat{T}_{inlet} = 280$ K, and the temperature at the outer surfaces of the bounding plates $\hat{\mathcal{T}}_C = 310$ K (from now on it will be indicated as the base temperature $\mathcal{T}_C = \hat{T}_{base} = 310$ K), whereas the inlet velocity $\hat{u}_{inlet}$ and the thermal conductivity of the stationary bounding layers k_s are varied from one simulation to another. Simulations are performed for both laminar and turbulent channel flows. In the latter, the steady Reynolds-averaged Navier–Stokes (RANS) method is used, implementing the realizable $k-\epsilon$ turbulence model, which guarantees high-quality modeling both away from and close to the wall. The choice of this turbulence model instead of the more widespread k-ω [27] resides in the fact that it showed a higher stability and convergence rate in our simulations. The software employed for mesh generation and numerical simulation are *Simcenter STAR-CCM+ 2302* (version 18.02.008-R8), for the cases in Sections 3.1 and 3.3.1, and *OpenFOAM* (version 10), for those in Sections 3.2 and 3.3.2. All the discretization schemes used are at least of second-order accuracy. For all the cases examined, the appropriateness of the mesh is confirmed by checking the available metrics, seeking for example sufficiently low values of non-orthogonality and skewness. Moreover, sample simulations are considered to check that the mesh is fine enough, especially near the channel boundaries, to guarantee that the conclusions are not affected by grid-resolution-related uncertainties. Special attention is directed to the turbulent airflow in the nose: the mesh is generated starting from a structured background with hexahedral cells of 0.5 mm edges, and then refinement is performed close to the walls reaching a size of 0.125 mm. Although it is non-trivial to assess the adequacy of proper mesh resolution in such a complex, non-planar geometry like the nasal airways, our near-wall mesh is fine enough to satisfy an average value of y^+ around 0.5.

3.1. Conjugate heat transfer in rough channels

Two-dimensional symmetric channels delimited by rough walls of four different textures are examined. The geometric details of the wall patterns are shown in Fig. 2. For each surface, the auxiliary systems (16) and (17) are solved over a periodic unit cell representative of the microscopic region to evaluate the closure fields $u_1^\dagger$ and $\theta^\dagger$, respectively; the integral/averaging relationships (18) and (19) are subsequently used to calculate the macroscopic coefficients λ_x, m_{12}, and λ_θ contributing to the effective velocity and temperature boundary conditions (10)–(13) at the fictitious interfaces passing by the crests of the protrusions. Solutions of the closure problems are provided in Fig. 3, taking the narrow triangle element as a representative example. The values obtained for the model coefficients are given in Table 1,

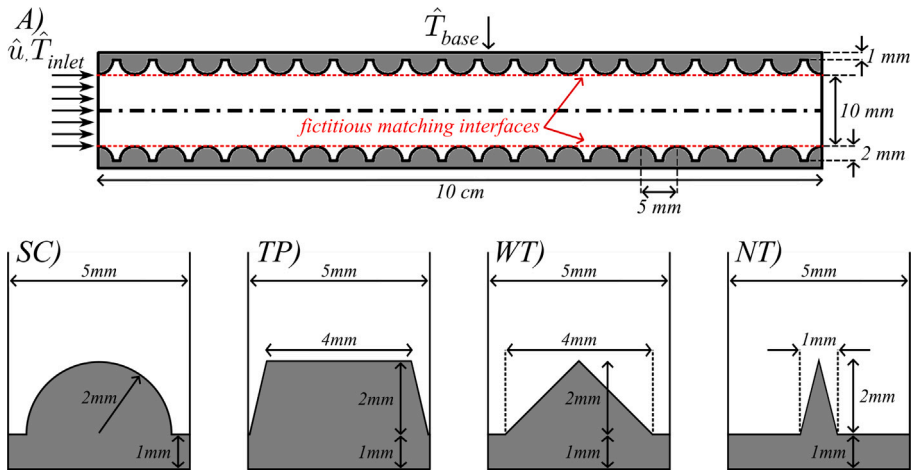

Fig. 2. Rough channel geometry and unit cells description. In (A) the dimensions of the domain are provided, and it is presented with the semicircular roughness elements. The dashed red line represents the fictitious matching interface where the homogenized boundary condition is applied. Full features and homogenized simulations are performed for four roughnesses. The geometries of the protrusions are: (SC) semicircular, (TP) trapezium, (WT) wide triangle and (NT) narrow triangle. All the unit cells are provided with dimensions.

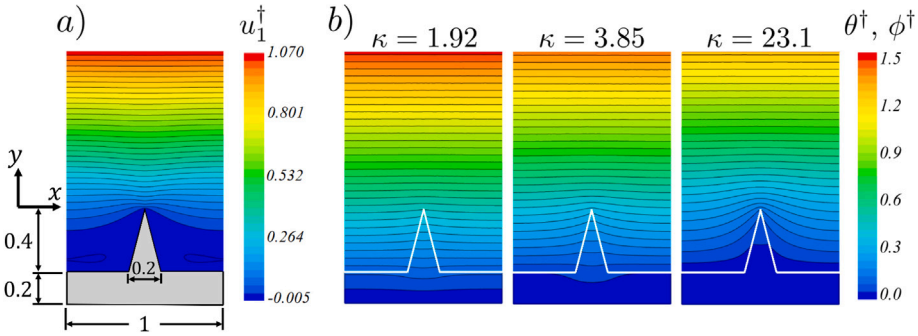

Fig. 3. Contours of the closure variables *(a)* $u_1^\dagger$ and *(b)* $\theta^\dagger$ and $\phi^\dagger$ for the case of a surface roughened with two-dimensional elements of triangular cross-section; cf. panel *(NT)* in Fig. 2. The geometry is sketched in dimensionless microscopic coordinates, with the pitch distance of the triangles used as a scale for normalization. Close-ups of the contours near the wall are displayed, while the typical unit cell considered in the simulations extends to $y \approx 5$.

Table 1
Dimensionless homogenized coefficients for the four wall textures sketched in Fig. 2. While λ_x and m_{12} are purely geometry-dependent, the thermal-slip coefficient λ_θ is also sensitive to the thermal conductivity ratio κ.

Config.	$\kappa\,(k_s/k_f)$	Dimensionless coeffs		
		λ_x	m_{12}	λ_θ
SC	1.92	0.0453	0.002211	0.3693
	3.85			0.2282
	23.1			0.0971
TP	1.92	0.0027	0.000034	0.3250
	3.85			0.1690
	23.1			0.0342
WT	1.92	0.0759	0.005693	0.4134
	3.85			0.2928
	23.1			0.1688
NT	1.92	0.0789	0.005735	0.4745
	3.85			0.3841
	23.1			0.2436

with the thermal-slip coefficient λ_θ calculated for different values of the solid-to-fluid thermal conductivity ratio κ.

Both fine-grained and homogenization-based simulations of the laminar flow in the channels are conducted with the inlet velocity $\hat{u}_{inlet} =$ 0.14 m/s. The Reynolds number evaluated based on the inlet velocity and the channel height (= 10 mm) is around 100. In Fig. 4, the numerical predictions of the homogenized simulations are validated against the running-average results calculated from the full CHT analysis, in terms of the temperature distributions along the fictitious interface and along plane of symmetry of the channel. The figure reveals that the upscaling approach employed permits accurate predictions for the macroscopic development of the thermal field along the channels, under different geometric conditions and thermal conductivity values of the rough boundaries.

3.2. Simplified model for smooth channels

Regarding the smooth channels, three different geometries are investigated: a straight channel, a convergent–divergent duct and an elbow pipe with a nozzle-like connection near the outlet, all characterized by a smooth surface interface between the solid layer and the fluid region. These specific geometries are chosen since they resemble shapes commonly found in the human nasal anatomy.

The geometrical parameters are presented in Fig. 5 and Table 2. Furthermore, to comprehensively explore the capabilities and limitations of the homogenized boundary condition, four solid layer thicknesses are examined for each case, particularly 1, 5, 10 and 15 mm while the solid-to-fluid thermal conductivity ratio is constant at $\kappa \approx 3.85$. Both laminar and turbulent flows are investigated: an inlet velocity to match a Reynolds number of 100 is applied to all the configurations (*SM*, *CD*,

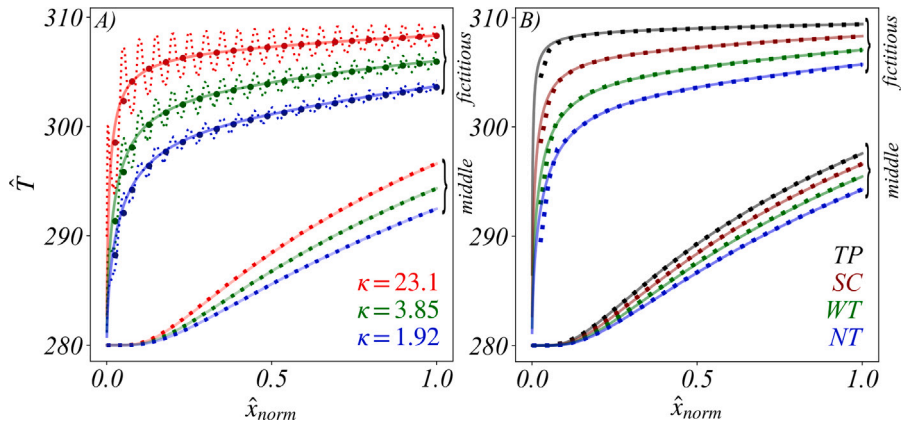

Fig. 4. Temperature distributions plotted against the normalized streamwise coordinate, along the fictitious interface and the centerline of the channel. In panel (A), semicircular roughness (SC in Fig. 2) is considered with three values of κ. Panel (B) shows the results for the roughness patterns sketched in Fig. 2, with κ = 23.1. The fluctuating dotted lines, superimposed in panel (A), represent the fully resolved temperature distributions along the fictitious interface. In both frames, the filled circles are the running averages of the temperature distributions resulting from the full simulations (refer to the definition in Eq. (6)), while the homogenized solutions are shown with solid lines.

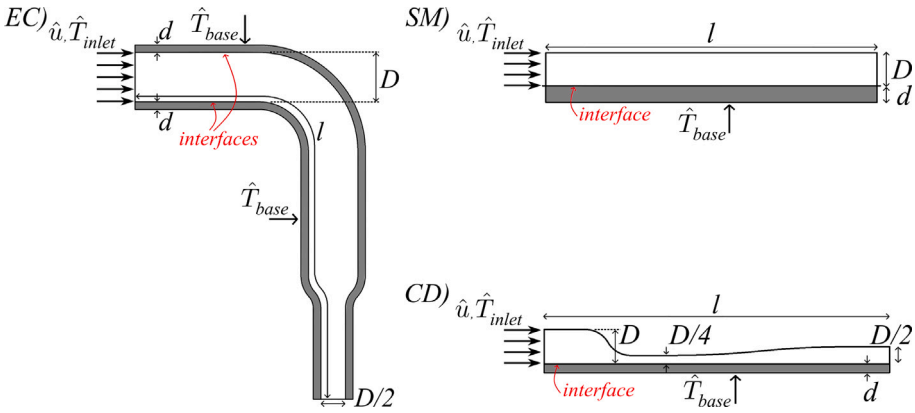

Fig. 5. The simple ducts for the smooth channels are characterized by: D channel diameter, d solid layer thickness, l channel length, $\hat{u}$, $\hat{T}_{inlet}$ inlet velocity and temperature and $\hat{T}_{base}$ the base temperature. (EC) the "elbow convergent" case, (SM) the smooth channel, (CD) the convergent–divergent duct. The upper boundary in channels (SM) and (CD) is adiabatic. For case *EC*, the radii of the upper and lower fluid-exposed surfaces of the elbow are fixed at 0.02 m and 0.01 m, respectively.

EC), while another set of simulations with an inlet velocity to match a Reynolds number of 4000 is run exclusively for the convergent–divergent geometry (*CD*). In Table 2, the inlet velocities assigned to achieve the desired Reynolds numbers are given. In Fig. 6, the temperature results for these cases are shown; a good agreement between the analytical model and the fully resolving simulations is found as long as the separation of scales is respected such that the simple effective condition of temperature (25) applies. It should be noticed that the normalized coordinate is defined as $\hat{s}_{norm} = \hat{s}/max(\hat{s})$, where $\hat{s}$ is the curvilinear coordinate. In *SM* and *CD*, $\hat{s}_{norm}$ coincides with the normalized streamwise coordinate, while in *EC* it is the normalized distance along the boundary of interest following its curvature. Additionally, the dimensionless temperature θ reported in the figure is given by $\theta = \dfrac{\hat{T} - \hat{T}_{inlet}}{\hat{T}_{base} - \hat{T}_{inlet}}$ such that its value is bounded between 0 and 1.

3.3. Complex ducts with a preferential heat transfer path

In this section, channels delimited by boundaries of complex geometries which are characterized by a preferential heat transfer path are analyzed. This means that the solid layer thickness, which is kept constant, should be sufficiently smaller compared to the other length scales such that heat transfer is favored in that direction of relatively lower thermal resistance. Under this condition, the effective temperature boundary condition (25) applies, and this can simplify the numerical analysis of the CHT.

Table 2
Characteristic dimensions of the channels sketched in Fig. 5 with inlet velocities.

Config	D [mm]	l [mm]	$\hat{u}_{inlet}$ [m/s]
EC	10	105	*lam* 0.15
SM	10	100	*lam* 0.15
CD	20	200	*lam* 0.075
			tur 3.0

3.3.1. Wavy-channel flow

Two undulating channels with preferential heat transfer path are analyzed here. Both have walls with large curvature; one is straight, and the other is convergent. The characteristic dimensions are shown in Fig. 7 along with the results of the full and the simplified simulations, performed with different values of the solid-to-fluid thermal conductivity ratio, κ. The inlet velocity is equal to 0.14 m/s, which corresponds to a Reynolds number of about 100 (Laminar). The results are evaluated both along the line of symmetry of the channel and along the inner surface of the bounding wall where the effective temperature

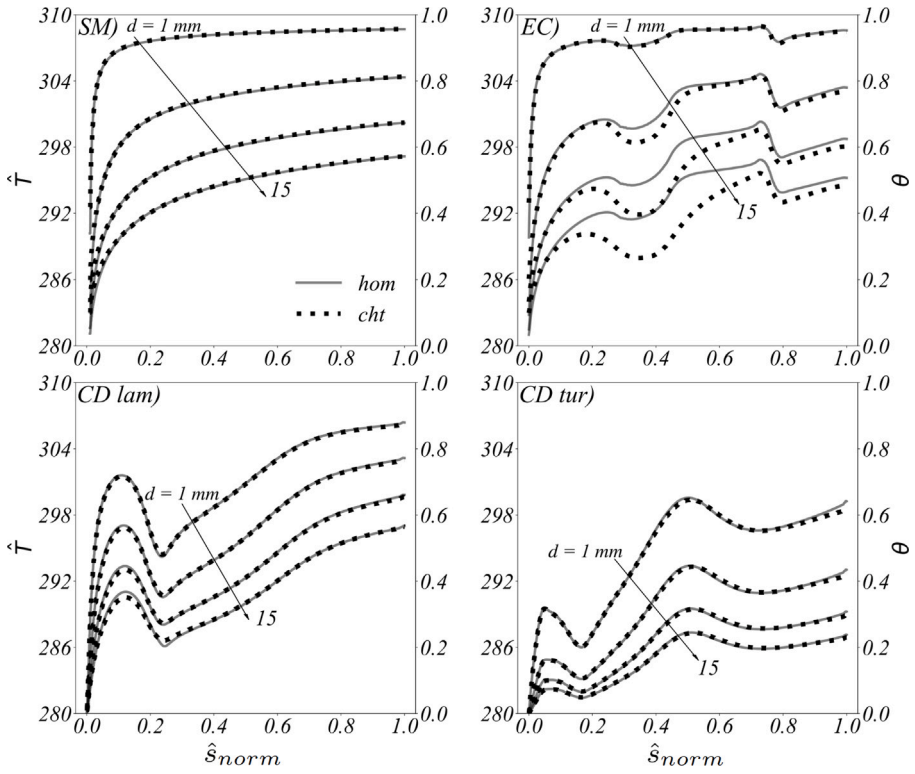

Fig. 6. The results for the smooth channels in Fig. 5 are presented here; four different thicknesses d are applied to the solid layer (1, 5, 10 and 15 mm). The dimensional and the non-dimensional temperatures ($\hat{T}$ on left ordinate and θ on right ordinate, respectively) are plotted against the normalized coordinate $\hat{s}_{norm}$. The sampling is performed at the solid–fluid interface. For (EC) sampling is performed at the lower interface.

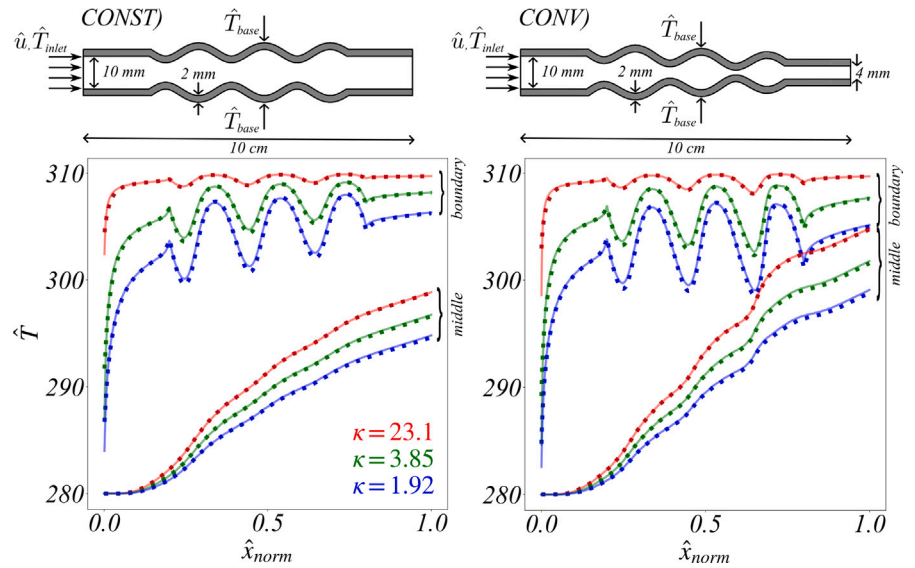

Fig. 7. Temperature results along the solid–fluid interface and the centerline of the channel for two complex geometries with a preferential heat transfer path and considering three different values of κ. The results are plotted against the normalized streamwise coordinate. (CONST) is characterized by a wavy pattern and the same height of the duct at inlet and outlet. (CONV) has the same waviness but is characterized by a smaller duct height at the outlet relative to the inlet. The circles show the results of the full CHT simulations, while the predictions with the effective temperature boundary condition are shown with solid lines. Reproducibility note: the first interface point in the simulations is located at a distance of order 0.1 mm from the inlet, reported to disclose the localized near-inlet grid-dependent effect.

boundary condition (25) is imposed. A good agreement is found for both geometries at all the values of κ considered.

3.3.2. Flow in the upper airways

A comparative analysis between the results obtained from the full CHT simulation of the nasal airflow and those generated employing the effective temperature boundary condition (25) at the interface between the mucous layer and the flowing air is presented here, with a specific focus on assessing the accuracy of the latter in modeling the air warming in the nasal airways. The present contribution connects to a previous work [28] on the nasal thermodynamics in which

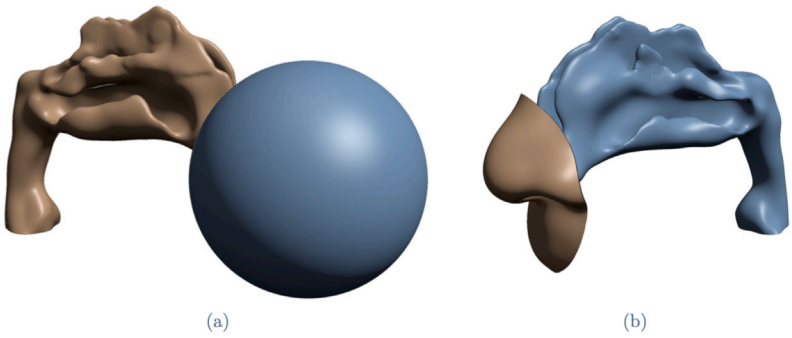

Fig. 8. 3D nose model including the external air volume around the nose tip (a) and the interface between the mucous layer and air region (b).

the CHT is studied and the turbulent flow is simulated via RANS as well as highly resolved LES. The motivation resides in the clinical significance of accurately identifying the coldest regions within the nasal cavity surface tissue, as they are associated with an elevated risk of bleeding. Notably, this phenomenon remains unaddressed when employing a uniform wall temperature boundary condition [19–21]. The patient-specific geometry is reconstructed starting from images acquired through Computed Tomography (CT) scan. A 3D model is produced using the software *3D Slicer* [29]. The procedure includes choosing a threshold for radiodensity levels [30] and smoothing the geometry to reduce the amount of details in order to achieve a meshable geometry [31]. In this study, the frontal and paranasal sinuses are removed. A spherical air volume surrounding the external nose is added to relocate the inlet area of the computational domain away from the nostrils, see Fig. 8. For the CHT simulation, the internal airways are bounded by an outer solid tissue whose thickness extends to a boundary where the internal body temperature is recovered. This thickness is taken as 0.5 mm, which is close to the value used in the work by Wu et al. [32]. As a side note, the tissue is two or three orders of magnitude thicker than the mucous layer alone. It is important to emphasize that some air passages are characterized by a diameter smaller than 1 mm and, therefore, the length scales are not perfectly separable there; this necessitates validation of the model. A constant temperature value of 310 K is imposed on the outer wall of the entire solid layer, based on the assumption that the network of the blood vessels beneath this layer is dense enough to keep the surrounding tissues at body temperature [33]. The stationary layer is modeled as a layer of water [28,32,34]. This simplification is reasonable since the mucous layer consists of 90%–95% water [35], and the underlying pseudo-stratified epithelium, which enables its production, is also rich in water. This stationary outer layer is omitted in other two simplified simulations where either a constant temperature (310 K) or the homogenization-based effective condition (25) is imposed at the boundary of the internal airways. The flow is forced at a constant rate of 16 l/min [36] (corresponding to a Reynolds number of 4000, evaluated at the throat based on the equivalent hydraulic diameter), the air enters the domain at a temperature $\hat{T}_{inlet} = 280$ K, and the solid properties for the tissue are given by $\rho = 993.36$ kg/m^3, $k_s = 0.598$ W/(m K), $c_v = 4181$ J/(kg K). It is worth mentioning that the air conditioning function of the nose is not limited to the mere warming/cooling of the air, but it also includes humidification [34,37]; the latent heat associated with evaporation/condensation is important to be taken into account towards a complete understanding of the nasal thermodynamics [16,38]. Inthavong et al. [15] found out that the latent heat energy transfer rate is almost one order of magnitude larger than the sensible heat effect. Nonetheless, the present work considers only the conductive–convective heat transfer in the nose taking its geometry as an example of complex ducts, mainly to validate the upscaled model and highlight its advantage. It is however encouraging to incorporate the role of moisturizing in the numerical framework for future research, which necessitates coupling with governing equations of the mass transfer in addition to possible adjustment of the effective temperature condition, depending on the case under study. The *OpenFOAM* utilities `blockMesh` and `snappyHexMesh` are used to generate the computational mesh. Quality is assured using a maximum skewness of 4 and a maximum non-orthogonality of 55°, with a total mesh of 15.4 million cells (9.4M for the fluid domain, 6M for the solid). The mesh of the fluid region is the same in the full CHT simulation and the simplified ones, allowing for a node-by-node comparison between the results of the different approaches. In Fig. 9, the temperature values along the interface separating solid and fluid regions are shown, according to the simulation where the effective boundary condition (25) is applied. The greatest differences from the internal temperature of the body (i.e., 310 K) are observed on the surface of the nose directly in contact with the external environment and in the vestibular area; clearly, these regions are far from the naso-pharynx in which the approximation of a constant interface temperature of 310 K can be considered acceptable. As also noted in [28], there is a wall temperature drop to around 306 K ($\approx$ 33 °C) at the beginning of the middle and inferior turbinates. The results obtained from the homogenized simulation are validated against those obtained from the full CHT simulation by computing the differences between the two corresponding temperature fields. As can be seen from Fig. 10, the homogenized boundary condition works well in reproducing the effect of the mucous layer without the need to simulate thermal conduction through it. In fact, within the computational fluid domain, temperature differences are between 0 K and $\pm$0.1 K, with the maximum temperature discrepancy being around 0.3 K in the coronal section number 3. This corresponds to a difference of 1% relative to the temperature jump present within the domain (i.e., $\hat{T}_{base} - \hat{T}_{inlet}$) which is equal to 30 K. In general, the biggest differences occur where the surface curvature is very high or in the narrower sections. For a better interpretation of the accuracy levels, we also compare the full CHT analysis with the simplest simulation in which a uniform temperature of 310 K is imposed at the interface between the air and mucous layer. As illustrated in Fig. 11, more significant differences can be observed (compared to those reported in 10), reaching up to 2 K. These differences are observed mainly in the vestibule, the nasal cavity and the beginning of the turbinates.

4. Discussion

The results presented above show that the upscaling theory adopted can be successfully applied to conjugate forced convection problems in channels delimited by perturbed walls (Section 3.1); the theory can be easily extended to the smooth-channel limit (Section 3.2) where an analytical solution for the thermal-slip coefficient can be found. Simple cases show good behavior of the model even if the hypothesis of separation of scales does not perfectly apply, while when this is accompanied by geometry complications (here, the elbow pipe case in Fig. 6-*EC*) careful attention should be paid to the assessment of applicability of

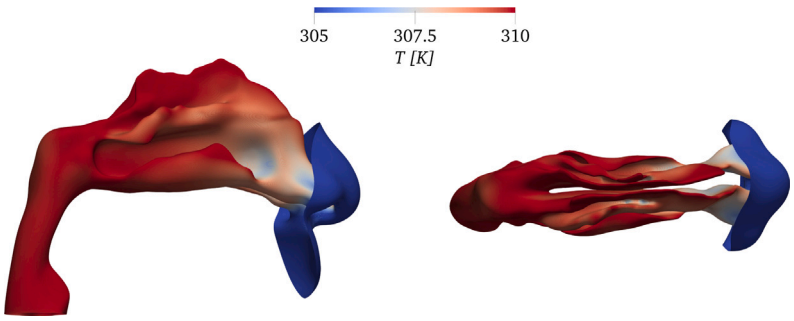

Fig. 9. Temperature distribution over the mucus–air interface, evaluated from the homogenization-based simulation.

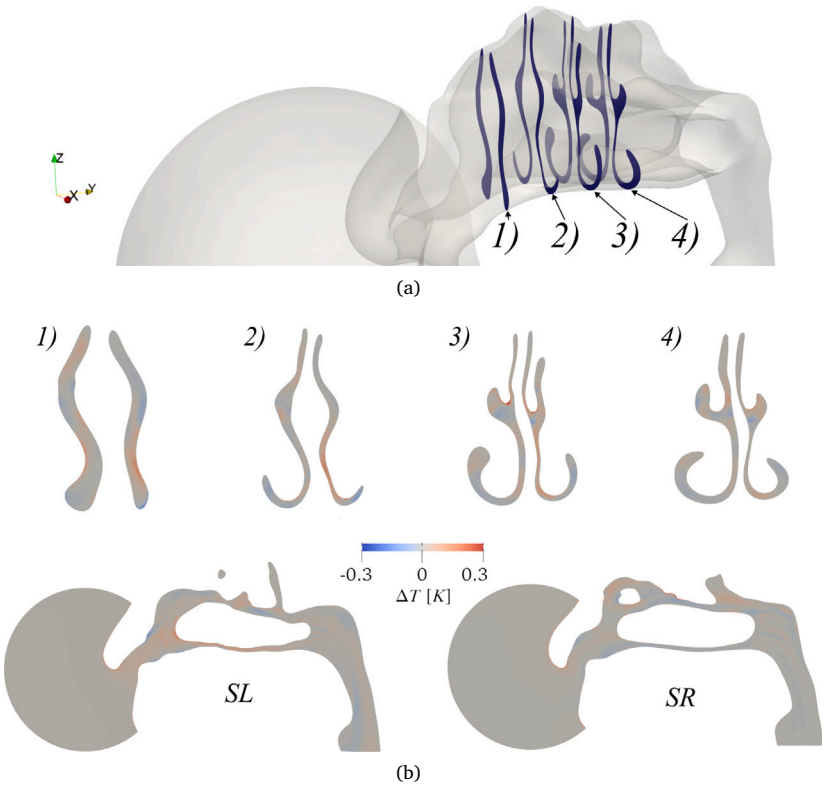

Fig. 10. Deviation of the homogenization-based prediction for the temperature field from the reference solution of the full CHT analysis. The differences ($T_{HOM} - T_{CHT}$) are displayed on four coronal sections (1–4) and on sagittal slices across left (SL) and right (SR) nostrils.

the theory. The plots in Fig. 6-*CD lam* clarify the agreement between the results of the model and the fine-grained simulations in a channel with a sudden decrease in the cross-sectional area. In the initial segment of the channel (up to $\hat{s}_{norm} \approx 0.1$), having a constant area, the temperature at the interface increases along with the development of the thermal boundary layer. In the region of sudden contraction, thinning of the thermal boundary layer is experienced (higher magnitudes of the negative temperature gradient at the wall) as the cold air stream is pushed down towards the interface. As a result, the temperature at the interface drops in this part of the channel, which can be easily inferred from the effective relationship (25). It is also interesting to highlight that in Fig. 6-*CD tur* the levels of temperature along the interface are lower due to the higher air mass flow rate through the channel and the improved heat exchange between fluid layers under turbulence. Within the range of applicability of the model, the predictions are in very good agreement with results of the fine-grained simulations even for complex structures of the boundaries (cf. Section 3.3). In Fig. 12, the dependence of the average temperature at the channel outlet on the thickness of the heated wall is displayed for each of the cases studied in Section 3.2, i.e. (SM) the smooth channel; (EC) the "elbow convergent" case; (CD) the convergent–divergent duct under either laminar (lam) or turbulent (tur) flow conditions. The model predictions are validated against results of the fully resolving simulations, and reasonable accuracy levels are found. The corresponding values of the relative error in the model predictions for the averaged dimensionless temperature, θ, at the outlet are summarized in Table 3. In Table 4, values of the RMSE (in its normalized version) of θ evaluated on the interface are provided for the simple ducts with the four tested thicknesses. This quantity is defined as:

$$RMSE = \sqrt{\frac{1}{N}\sum_{i=1}^{N}\left(\frac{\theta_{hom-i} - \theta_{cht-i}}{\theta_{cht,mean}}\right)^2} \times 100\,[\%] \tag{26}$$

where θ_{hom-i} and θ_{cht-i} are the non-dimensional temperatures and i refers to each sampling point on the interface, N is the total number of samples and $\theta_{\mathrm{cht,mean}}$ denotes the mean value of θ_{cht} along the interface of interest. While the errors are marginal for the majority

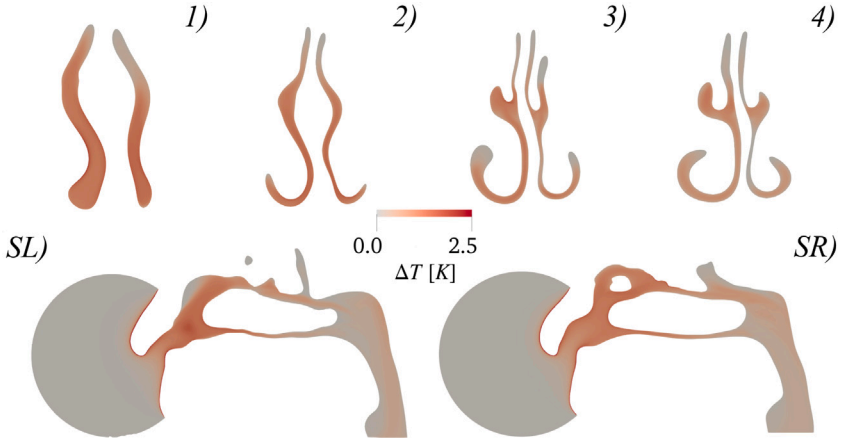

Fig. 11. Deviation of the temperature field prediction when a fixed temperature (310 K) is imposed at the mucus–air interface from the reference solution of the full CHT analysis. The differences ($T_{fix} - T_{CHT}$) are displayed on four coronal sections (1–4, as in Fig. 10) and on sagittal slices across left (SL) and right (SR) nostrils.

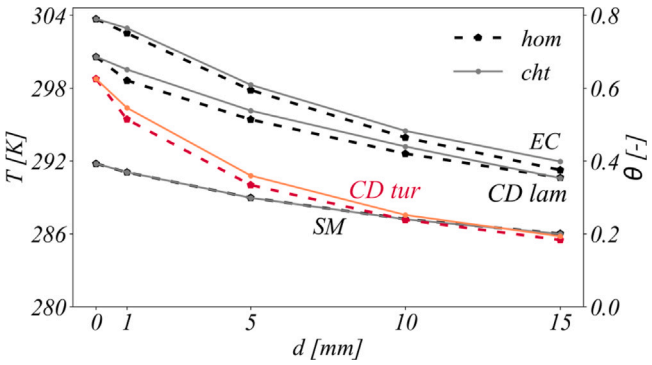

Fig. 12. Behavior of the average temperature on the outlet patch with the increase in the solid layer thickness (d), plotted for the four cases considered in Section 3.2.

of configurations, we highlight that considerable deviations between the model predictions and the reference results are realized in the elbow-convergent case with large thicknesses of the boundary (10 and 15 mm). This is expected (in view of point (iv) in the notes given in Section 2.3) and can be attributed to the large values of the thickness-to-radius ratio Γ (respectively, 2 and 3) with which the flat-interface assumption is no longer valid. Note: the results are accurate for e = 1 mm ($\Gamma \approx 0.1$) and for $e = 5$ mm ($\Gamma \approx 0.67$).

The following notes on the computational advantages of the effective model are worth highlighting.

i. The classical full simulation of the flow and the conjugate heat transfer in channels bounded by rough walls can be computationally demanding, due to the required expensive numerical resolution of the fields near and within the features of the ribbed boundaries. The homogenization-based approach applied in Section 3.1 is, in contrast, concerned with the upscaled fields, where equivalent, macroscopic boundary conditions of the velocity and temperature are imposed at a plane virtual surface next to the physical rough wall. This can significantly alleviate the mesh requirements and accelerate the numerical study. The reader is referred to [26] where a quantitative analysis of the reduction in the mesh and the elapsed wall-clock time — including the time required to obtain the coefficients — is presented, although natural convection, and not forced conjugate convection, is investigated there. Another point is that structured mesh can be generated easily in the homogenized simulations, unlike the fully resolved ones.

ii. In the smooth-channel limiting case (i.e., in the absence of roughness elements) the mesh reduction and the time saving achieved by applying the model are of lesser significance since resolving conduction in the smooth solid layer is usually not very computationally demanding. However, this does not apply to a complex configuration like the nasal airflow, where the number of cells required to resolve the solid layer is large, primarily for geometrical reasons rather than for purely computational ones, in fact introducing a solid layer, of arbitrary thickness, in a very complex geometry introduces a series of meshing difficulties which scales with cell dimension, among which it

Table 3
Values of the average dimensionless temperature, θ, at the channel outlet, evaluated from the full conjugate heat transfer analysis (cht) and the homogenized model (hom), besides the corresponding percentage error in the model predictions ($\%\Delta$). The values given in the left column refer to the thickness of the heated wall, d.

		SM	$CD\,lam$	$CD\,tur$	EC
1 mm	cht [–]	0.369	0.621	0.084	0.750
	hom [–]	0.369	0.651	0.082	0.765
	$\%\Delta$ [–]	0.005	0.303	0.018	0.140
5 mm	cht [–]	0.299	0.514	0.034	0.595
	hom [–]	0.299	0.538	0.034	0.610
	$\%\Delta$ [–]	0.001	0.248	0.003	0.143
10 mm	cht [–]	0.241	0.420	0.025	0.464
	hom [–]	0.240	0.440	0.025	0.483
	$\%\Delta$ [–]	0.004	0.200	0.006	0.188
15 mm	cht [–]	0.200	0.354	0.022	0.375
	hom [–]	0.200	0.353	0.022	0.400
	$\%\Delta$ [–]	0.004	0.013	0	0.240

Table 4
The Root Mean Square Error (RMSE) in the model results for θ along the solid–fluid interface for the four simple ducts. The values given in the left column refer to the thickness of the heated wall, d.

	SM	$CD\,lam$	$CD\,tur$	EC
1 mm	0.38%	0.43%	2.23%	0.70%
5 mm	1.00%	0.75%	3.72%	3.12%
10 mm	1.40%	1.31%	5.10%	9.69%
15 mm	1.70%	4.06%	5.83%	19.83%

emerges the inability of accurately following the interface in case of small geometrical features which are inaccurately described when using a large cell; in the case of the nose, these difficulties emerged consistently and caused self-intersection problems, the collapse of the cells and many other mesh failure causes that motivate the need of using a large number of cells to accurately model the shape of the solid layer rather than for purely computational requirements. The geometrical requirements had a large impact on the final cell count which was then estimated once the equivalent boundary condition was implemented: the number of cells reduced by 39% and the RAM usage, during the simulation, reduced almost linearly of a 40%. It is also worth noting that, along with the cell and RAM usage, also the computational time reduced by, around, 20%.

5. Conclusions

In the present contribution, an upscaling method is applied to the problem of internal, pressure-driven, developing flow with conjugate heat transfer. Macroscopic boundary conditions of the velocity and temperature are adopted and validated on different roughness patterns. The implementation of this typical effective framework under the preceding conditions represents a significant advancement to homogenization-based modeling. Besides, we consider the smooth-channel limiting scenario for which an analytical expression of the thermal-slip coefficient can be easily derived. This special, simplified version of the model is tested on simple and complex-shaped ducts, from arbitrary two-dimensional channels up to a biological configuration, i.e., the upper respiratory tract of a human. The results obtained exhibit, in general, a strong agreement with the classical fully resolving simulations. For the human nose case, the error in the temperature field across the whole domain is found to be below 1%, which emphasizes the advantage of the Robin temperature boundary condition as an accurate, cheaper alternative to the full conjugate heat transfer analysis in practical applications. Moreover, it permits an easier pre-processing of complex geometries by allowing us to eschew the introduction of the solid layer; this yields a more robust computational setup whenever the problem of interest is geometrically complex.

In light of the rediscovery of multiscale homogenization in recent years and the growing number of studies on its application to a variety of physically relevant problems, we believe that this paper opens up new perspectives for the implementation of the theory. In particular, it is encouraging to work on more sophisticated homogenization-based approaches for multiphysics modeling; this permits a wider applicability of the theory to practical engineering problems. Moreover, it would be interesting to employ the effective boundary conditions resulting from these approaches to accelerate large-scale optimization studies of the wall texture/topology in pursuit of improving the performance of thermal and fluid transportation systems.

CRediT authorship contribution statement

Eric Segalerba: Writing – review & editing, Writing – original draft, Methodology, Investigation, Conceptualization. **Essam Nabil Ahmed:** Writing – review & editing, Writing – original draft, Methodology, Investigation, Conceptualization. **Maria Vittoria Pennisi:** Writing – original draft, Investigation. **Maurizio Quadrio:** Writing – original draft, Supervision, Investigation, Conceptualization. **Jan Oscar Pralits:** Writing – review & editing, Writing – original draft, Methodology, Investigation, Conceptualization.

Declaration of competing interest

The authors declare that they have no known competing financial interests or personal relationships that could have appeared to influence the work reported in this paper.

Data availability

Data will be made available on request.

References

[1] M.T. Lewis, J.P. Hickey, Conjugate heat transfer in high-speed external flows: A review, J. Thermophys. Heat Transfer 37 (2023) 697–712, http://dx.doi.org/10.2514/1.T6763.
[2] F.J. Hong, P. Cheng, H. Ge, G.T. Joo, Conjugate heat transfer in fractal-shaped microchannel network heat sink for integrated microelectronic cooling application, Int. J. Heat Mass Transfer 50 (2007) 4986–4998, http://dx.doi.org/10.1016/j.ijheatmasstransfer.2007.09.006.
[3] F. Duchaine, A. Corpron, L. Pons, V. Moureau, F. Nicoud, T. Poinsot, Development and assessment of a coupled strategy for conjugate heat transfer with large eddy simulation: Application to a cooled turbine blade, Int. J. Heat Fluid Flow 30 (2009) 1129–1141, http://dx.doi.org/10.1016/j.ijheatfluidflow.2009.07.004.
[4] N.S. Bondareva, M.A. Sheremet, Conjugate heat transfer in the PCM-based heat storage system with finned copper profile: Application in electronics cooling, Int. J. Heat Mass Transfer 124 (2018) 1275–1284, http://dx.doi.org/10.1016/j.ijheatmasstransfer.2018.04.040.
[5] B.J. Jeon, H.G. Choi, Numerical analysis for the conjugate heat transfer of skin under contrast therapy, Int. J. Heat Mass Transfer 86 (2015) 388–396, http://dx.doi.org/10.1016/j.ijheatmasstransfer.2015.03.019.
[6] P. Kishore, S. Kumar, V.M. Patel, Conjugate heat transfer analysis of laser-irradiated cylindrical-shaped biological tissue embedded with the optical inhomogeneity, Int. Commun. Heat Mass Transfer 137 (2022) 106302, http://dx.doi.org/10.1016/j.icheatmasstransfer.2022.106302.
[7] I. Babuška, Homogenization and its application: Mathematical and computational problems, Numer. Solut. Partial. Differ. Equations – III (1976) 89–116, http://dx.doi.org/10.1016/B978-0-12-358503-5.50009-9.
[8] A. Bottaro, Flow over natural or engineered surfaces: An adjoint homogenization perspective, J. Fluid Mech. 877 (2019) P1, http://dx.doi.org/10.1017/jfm.2019.607.
[9] G.A. Zampogna, J. Magnaudet, A. Bottaro, Generalized slip condition over rough surfaces, J. Fluid Mech. 858 (2019) 407–436, http://dx.doi.org/10.1017/jfm.2018.780.
[10] S.J. Bolaños, B. Vernescu, Derivation of the Navier slip and slip length for viscous flows over a rough boundary, Phys. Fluids 29 (2017) 057103, http://dx.doi.org/10.1063/1.4982899.
[11] A. Bottaro, S.B. Naqvi, Effective boundary conditions at a rough wall: A high-order homogenization approach, Meccanica 55 (2020) 1781–1800, http://dx.doi.org/10.1007/s11012-020-01205-2.
[12] E.N. Ahmed, A. Bottaro, G. Tanda, A homogenization approach for buoyancy-induced flows over micro-textured vertical surfaces, J. Fluid Mech. 941 (2022) A53, http://dx.doi.org/10.1017/jfm.2022.320.
[13] E.N. Ahmed, A. Bottaro, G. Tanda, Conjugate natural convection along regularly ribbed vertical surfaces: A homogenization-based study, Numer. Heat Transf. Part A: Appl. 85 (2023) 1331–1355, http://dx.doi.org/10.1080/10407782.2023.2202347.
[14] E.N. Ahmed, G. Tanda, An experimental and numerical study of laminar natural convection along vertical rib-roughened surfaces, Int. J. Heat Mass Transfer 223 (2024) 125227, http://dx.doi.org/10.1016/j.ijheatmasstransfer.2024.125227.
[15] K. Inthavong, D.F. Fletcher, M. Khamooshi, S. Vahaji, H. Salati, Wet surface wall model for latent heat exchange during evaporation, Int. J. Numer. Methods Biomed. Eng. 38 (2022) e3581, http://dx.doi.org/10.1002/cnm.3581.
[16] S. Hanida, F. Mori, K. Kumahata, M. Watanabe, S. Ishikawa, T. Matsuzawa, Influence of latent heat in the nasal cavity, J. Biomech. Sci. Eng. 8 (2013) 209–224, http://dx.doi.org/10.1299/jbse.8.209.
[17] Y. Na, S.-K. Chung, S. Byun, Numerical study on the heat-recovery capacity of the human nasal cavity during expiration, Comput. Biol. Med. 126 (2020) 103992, http://dx.doi.org/10.1016/j.compbiomed.2020.103992.
[18] S.-K. Chung, Y. Na, Dynamic characteristics of heat capacity of the human nasal cavity during a respiratory cycle, Respir. Physiol. Neurobiol. 290 (2021) 103674, http://dx.doi.org/10.1016/j.resp.2021.103674.
[19] G. Garcia, N. Bailie, D. Martins, J. Kimbell, Atrophic rhinitis: A CFD study of air conditioning in the nasal cavity, J. Appl. Physiol. (Bethesda, Md. : 1985) 103 (2007) 1082–1092, http://dx.doi.org/10.1152/japplphysiol.01118.2006.
[20] P.H. Saksono, P. Nithiarasu, I. Sazonov, Numerical Prediction of Heat Transfer Patterns in a Subject-Specific Human Upper Airway, J. Heat Transf. 134 (2012) 031022, http://dx.doi.org/10.1115/1.4005158.
[21] J. Kimbell, D. Frank-Ito, P. Laud, G. Garcia, J. Rhee, Changes in nasal airflow and heat transfer correlate with symptom improvement after surgery for nasal obstruction, J. Biomech. 46 (2013) 2634–2643, http://dx.doi.org/10.1016/j.jbiomech.2013.08.007.
[22] K. Kumahata, F. Mori, S. Ishikawa, T. Matsuzawa, Nasal flow simulation using heat and humidity models, J. Biomed. Sci. Eng. 5 (2010) 565–577, http://dx.doi.org/10.1299/jbse.5.565.

[23] J. Bibin, P. Senthilkumar, S. Sadasivan, Applied and theoretical aspects of conjugate heat transfer analysis: A review, Arch. Comput. Methods Eng. 26 (2018) 475–489, http://dx.doi.org/10.1007/s11831-018-9252-9.

[24] H. Stone, A. Stroock, A. Ajdari, Engineering flows in small devices: Microfluidics towards a lab-on-a-chip, Annu. Rev. Fluid Mech. 36 (2004) 381–411, http://dx.doi.org/10.1146/annurev.fluid.36.050802.122124.

[25] E.N. Ahmed, A. Bottaro, Laminar flow in a channel bounded by porous-rough walls: Revisiting beavers-joseph-saffman, Eur. J. Mech. B Fluids 103 (2024) 269–283, http://dx.doi.org/10.1016/j.euromechflu.2023.10.012.

[26] E.N. Ahmed, Natural-convection heat transfer from regularly ribbed vertical surfaces: Homogenization-based simulations towards a correlation for the nusselt number, Numer. Heat Transf. Part A: Appl. 83 (2023) 991–1013, http://dx.doi.org/10.1080/10407782.2023.2165993.

[27] Z. Zhang, C. Kleinstreuer, Laminar-to-turbulent fluid–nanoparticle dynamics simulations: Model comparisons and nanoparticle-deposition applications, Int. J. Numer. Methods Biomed. Eng. 27 (2011) 1930–1950, http://dx.doi.org/10.1002/cnm.1447.

[28] F. Mangani, Effetto Della Temperatura Nella Fluidodinamica Nasale, (Master's thesis), Politecnico di Milano, 2019-2020.

[29] A. Fedorov, R. Beichel, J. Kalpathy-Cramer, J. Finet, J.-C. Fillion-Robin, S. Pujol, C. Bauer, D. Jennings, F. Fennessy, M. Sonka, J. Buatti, S. Aylward, J.V. Miller, S. Pieper, R. Kikinis, 3D slicer as an image computing platform for the quantitative imaging network, Magn. Reson. Imaging 30 (2012) 1323–1341, http://dx.doi.org/10.1016/j.mri.2012.05.001.

[30] M. Quadrio, C. Pipolo, S. Corti, F. Messina, C. Pesci, A.M. Saibene, S. Zampini, G. Felisati, Effects of CT resolution and radiodensity threshold on the CFD evaluation of nasal airflow, Med. Biol. Eng. Comput. 54 (2016) 411–419, http://dx.doi.org/10.1007/s11517-015-1325-4.

[31] E. Segalerba, G.D. Ciacci, M. Quadrio, J.O. Pralits, On the comparison between pre- and post-surgery nasal anatomies via computational fluid dynamics, Biomech. Model. Mechanobiol. 23 (2023) 305–314, http://dx.doi.org/10.1007/s10237-023-01776-5.

[32] D. Wu, M. Tawhai, E. Hoffman, C. Lin, A numerical study of heat and water vapor transfer in MDCT-based human airway models, Ann. Biomed. Eng. 40 (2014) 2117–2131, 10.1007%2Fs10439-014-1074-9.

[33] F. MacArthur, G. McGarry, The arterial supply of the nasal cavity, Eur. Arch. Otorhinolaryngol. 274 (2017) 809–815, http://dx.doi.org/10.1007/s00405-016-4281-1.

[34] D.-W. Kim, S.-K. Chung, Y. Na, Numerical study on the air conditioning characteristics of the human nasal cavity, Comput. Biol. Med. 86 (2017) 18–30, http://dx.doi.org/10.1016/j.compbiomed.2017.04.018.

[35] R. Bansil, B.S. Turner, The biology of mucus: Composition, synthesis and organization, Adv. Drug Deliv. Rev. 124 (2018) 3–15, http://dx.doi.org/10.1016/j.addr.2017.09.023.

[36] D. Wang, H. Lee, R. Gordon, Impacts of fluid dynamics simulation in study of nasal airflow physiology and pathophysiology in realistic human three-dimensional nose models, Clin. Exp. Otorhinolaryngol. 5 (2012) 181–187, http://dx.doi.org/10.3342/ceo.2012.5.4.181.

[37] T. Keck, R. Leiacker, A. Heinrich, S. Kühnemann, G. Rettinger, Humidity and temperature profile in the nasal cavity, Rhinology 38 (2001) 167–171.

[38] H. Shamohammadi, S. Mehrabi, S. Sadrizadeh, M. Yaghoubi, O. Abouali, 3D numerical simulation of hot airflow in the human nasal cavity and trachea, Comput. Biol. Med. 147 (2022) 105702, http://dx.doi.org/10.1016/j.compbiomed.2022.105702.